



D6.4 – Mechanical design plans & simulation results of the integration of the power electronics converters into an e-axle and a battery pack

SWITCHING-CELL-ARRAY-BASED POWER ELECTRONICS CONVERSION FOR FUTURE ELECTRIC VEHICLES

DATE: 15 January 2026

VERSION: 2.0

Author(s): Mattia Grespan, Ludovico Campanelli (UM)

Contributor(s): Àlber Filbà (IREC), Sergio Busquets (UPC), Diego Angeli, Davide Barater (UM)

Project: SCAPE | www.scapepower.eu

Project duration: 01.07.2022 – 30.06.2026

Grant Agreement N°: 101056781

Coordinator: Àlber Filbà (IREC)

Email: afilba@irec.cat

Dissemination level: Public

Work package: WP6

Description: This deliverable provides a report of the integration of the power converters into an e-axle configuration and into the traction battery, and the simulation data that verifies its feasibility.



Document History

Date	Contributors	Action	Status
4 July 2025	M. Grespan, L. Campanelli (UM)	Writing of a first draft version of the document	Draft (V0.1)
21 October 2025	À. Filbà (IREC)	Consolidation of the document, ready for review phase	Review (V1.0)
15 November 2025	G. Fañanás (UPC), O. Esquiús (IREC)	Review for corrections	Review (V1.1)
3 December 2025	M. Grespan, L. Campanelli (UM)	Abridged version of the document	Review (V1.2)
15 January 2026	À. Filbà (IREC)	Final revision	Final (V2.0)



Executive Summary

This document studies the integration of the SCAPE integrated inverter-charger (IIC) converter into the EV electric motor and the integration of the battery-interfacing converter (BIC) into the EV battery. The thermal management of both integrated systems is studied by developing lumped parameter thermal networks. These thermal models are used to assess the feasibility of the proposed integrated designs from the thermal point of view. Mechanical designs of the converters assembly into the motor and battery are provided and are employed to define the lumped parameters in the thermal models.

The first part of this document covers the thermal analysis of the integrated assembly composed of the electric motor and IIC power converter. To this end, three lumped parameter thermal models are developed, which are then combined with a CFD model of the cooling jacket to evaluate hot-spot temperatures in the most relevant components of the assembly. In addition, a sensitivity analysis is performed to identify possible thermal performance improvements achievable by selecting different constitutive materials from some components of the assembly.

In the second part of the document analogous thermal models are developed for the battery pack and BIC converter.

In both cases the temperatures of most relevant components are below their safety limits, thus confirming the feasibility of the two proposed integrated architectures.



List of Figures

Figure 1 – Schematic representing the integrated assembly composed by the electric motor and the IIC.....	10
Figure 2 – Arrangement of nodes and thermal resistances constituting the two-dimensional thermal model of the electric motor integrated with the IIC.....	13
Figure 3 – Values of AC/DC loss ratios K_{rk} as a function of frequency for all conductor layers in the active section of the motor, and in the end-windings.....	13
Figure 4 – Longitudinal section of the 3D LPTN of a single slot positioned at the centerline of the windings.....	15
Figure 5 – Thermal connections between winding layers.....	15
Figure 6 – Thermal connections between coolant nodes.....	15
Figure 7 – Schematic showing the front face of the complete three-dimensional thermal Model of the integrated motor and converter assembly.....	16
Figure 8 – Comparison between the temperature values of the windings and stator iron obtained from the LPTN and FE models.....	17
Figure 9– Selected views of the computational mesh of the CFD model developed for the cooling jacket.....	18
Figure 10 – Colourmaps of dimensionless velocity magnitude and temperature difference on a transversal cross-section of the cooling jacket.....	19
Figure 11 – Distributions of temperature and heat fluxes in the stator of the electric machine, obtained from the two-dimensional thermal model of the integrated assembly.....	20
Figure 12 – Distributions of winding temperatures along axis of the motor, obtained from the 3D single-slot model (left) and complete 3D LPTN (right).....	20
Figure 13 – Temperature contour plot of the stator and rotor obtained on a cross-section located at the center of the motor, considering numerical results from the complete 3D thermal model.....	21
Figure 14 – Contour plots of dimensionless temperature difference on the stator, obtained from the sensitivity analyses performed on the most relevant constitutive parameters associated with the stator of the motor.....	24
Figure 15 – Contour plots of dimensionless temperature difference on the rotor, obtained from the sensitivity analyses performed on the most relevant constitutive parameters associated with the rotor of the motor.....	25
Figure 16 – Contour plots of dimensionless temperature difference on the power converter, obtained from the sensitivity analyses performed on the most relevant constitutive parameters associated with power converter.....	25
Figure 17 – Scheme of the cooling channels.....	27
Figure 18 – Three-dimensional view of one of the four plate coolers and cell stack forming the integrated battery pack and BIC power converter, whose components are mounted on the bottom of the plate cooler.....	27
Figure 19 – Thermal network of the modules and cooling channels.....	28
Figure 20 – Thermal network of a) LVSC single leg, b) HVSC single leg, c) transformer.....	28
Figure 21 – Losses of a single LV leg.....	28
Figure 22 – Traction inverter current at its dc port for a WLTP driving cycle. A negative current indicates discharging of the battery.....	28
Figure 23 – C-rate profile.....	28
Figure 24 – SOC of the two packs.....	29



Figure 25 – Temperature profiles of the first and last module of each battery pack30

Figure 26 – Colormap showing the maximum temperature reached at each sector of the battery thermal model.30

Figure 27 – Temperature of the battery modules underneath the high-voltage (HV) and low-voltage (LV) BIC boards.30

Figure 28 – Temperature profiles of BIC components.....30



List of Tables

Table 1 – Values of thermal conductivity of the materials associated with the main components of the electric motor.....	11
Table 2 – Losses produced by the stator and rotor laminations, and permanent magnets.....	12
Table 3 – Values of conduction, switching, and overall losses associated with each SC.....	14
Table 4 – Boundary conditions applied to the thermal models developed for the integrated assembly under examination.....	16
Table 5 – Expected and numerical values of bulk temperature difference obtained from the two three-dimensional thermal models. Values in °C.....	17
Table 6 – Numerical results from the mesh sensitivity analysis and from Richardson’s extrapolation.....	18
Table 7 – Hot-spot temperature results associated with the main components of the assembly, and obtained from the three lumped parameters thermal models.....	20
Table 8 – Values of thermal conductivity of the materials associated with the main components of the electric motor and power converter. Values of λ in W/(mK), values of U in W/(m ² K), and values of R in °C/W	22
Table 9 – Battery pack data.....	26



List of Acronyms and Abbreviations

2D	Two-dimensional
3D	Three-dimensional
AB	Advisory Board
BIC	Battery Interfacing Converter
CFD	Computational Fluid Dynamics
DES	Dissemination and Exploitation Strategy
EB	Executive Board
EC	European Commission
EIB	Exploitation and Innovation Board
EV	Electric Vehicle
GA	General Assembly
IIC	Integrated Inverter Charger
IPR	Intellectual Property Rights
HF	High Frequency
HTC	Heat Transfer Coefficient
HV	High Voltage
LPTN	Lumped Parameter Thermal Network
LV	Low Voltage
ML-DAB	Multilevel Dual Active Bridge
OA	Open Access
OEM	Original Equipment Manufacturer
PC	Project Coordinator
PCB	Printed Circuit Board
SC	Switching Cell
SOC	State of Charge
WP	Work Packages



Contents

Document History	1
Executive Summary	2
List of Figures.....	3
List of Tables	5
List of Acronyms and Abbreviations.....	6
1. Introduction.....	8
2. Integration of the IIC with the electric motor	9
2.1. Case study.....	9
2.2. Numerical methods	10
2.2.1. Two-dimensional thermal model.....	10
2.2.2. 3D single-slot thermal model.....	14
2.2.3. Complete 3D thermal model	15
2.2.4. Boundary conditions and implementation	16
2.2.5. Validation of advective thermal resistances and thermal diodes	16
2.2.6. Validation of the 2D motor thermal model.....	17
2.2.7. Numerical model of the cooling jacket.....	17
2.3. Results.....	19
2.3.1. Parameter sensitivity analysis.....	21
3. BIC Integration	26
3.1. LPTN model	26
3.2. Results.....	29
4. Conclusion	31
5. References.....	32
5.1. SCAPE documents	32
5.2. Citations.....	32



1. Introduction

The first part of this document discusses the thermal analysis of the integrated assembly composed of the electric motor and IIC [1] power converter. The developed thermal modelling approach is based on lumped parameters thermal networks developed on the basis of nominal geometric parameters, tabled material properties, established empirical correlations, and numerical results obtained from CFD and FE models. Numerical hot-spot temperature results stemming from the three LPTN thermal models are compared, while discussing the benefits and drawbacks of each model in terms of accuracy, development time, and computational effort. Subsequently, a sensitivity analysis is performed to evaluate possible improvements to the thermal management of assembly that could be attained by selecting different constitutive materials for some components of the assembly

The second part of Task 6.3 concerns the virtual integration of the BIC with the energy storage system. The total energy is almost 100 kWh, obtained by connecting 2 battery packs in series, each containing 248 modules in an 8S31P configuration, with each module comprising 26 cells in a 13S2P configuration. The first battery pack is connected to the BIC, for this reason the current input splitting is managed by a controller which aims to balance the SOC of the two packs. The BIC consists of ML-DAB DC-DC converter that controls the power flow between the high-voltage traction battery and the low-voltage service battery feeding vehicle low-voltage loads. The temperatures of the batteries and the BIC are managed by a liquid cooling plate with two parallel serpentine channels. This configuration maintains good temperature uniformity without significantly increasing pressure losses due to coolant flow. The overall system (batteries, cooling-plate and BIC) is modelled using a LPTN, where each module is a node, and the cooling channels are represented by additional nodes connected by an advective resistance to model fluid heating as it flows. Regarding the BIC, each SC is represented by a node connected to the copper layer via the thermal junction resistance. Finally, the results for a drive cycle test are presented.

This document is organized as follows: Section 0 is devoted to the integration of the IIC with the electric motor; Section 3 presents the modeling strategy and simulation results of the BIC integration with the energy storage system. Finally, Section 4 presents the conclusions.



2. Integration of the IIC with the electric motor

2.1. Case study

The integrated assembly under consideration consists of a six-phase permanent magnet synchronous motor and the associated power converter. The stator of the electric machine is made out of NO20-1200H laminated electrical steel, its external and internal radii are $r_{s,ext} = 132.15$ mm and $r_{s,int} = 96.0$ mm, respectively. The motor presents an active length of $l_s = 140$ mm. The stator houses 96 rectangular slots, which have a width of $w_{sl} = 3.6$ mm and a height of $h_{sl} = 17.2$ mm. Each slot is lined with Kapton®-based insulating paper with a thickness of $t_p = 0.22$ mm. At the base of the slots the paper is folded, forming a layer of insulation with a thickness of 0.44 mm. The copper windings present a hairpin arrangement, including six conductor layers with varying cross-section. All the copper busbars have a rectangular cross section with a width of $w_c = 2.8$ mm, while they present different height-values depending on their position: the four conductors closest to the rotor have a height of $h_{c,sh} = 1.8$ mm, while the two furthest away have a height of $h_{c,ta} = 4.0$ mm. The vertical spacing between two conductors is 0.245 mm. The bus bars are enamelled with a layer of Voltatex® insulating compound that has a thickness of $t_e = 0.0725$ mm, and the space between them is filled with SbTCM resin. All the materials used for the insulation of the windings are H-class rated, meaning that the maximum working temperature of the windings is 180 °C. The rotor features two types of neodymium-iron-boron magnets having the same width of $w_m = 11$ mm, and heights of $h_{m,ta} = 5.5$ mm and $h_{m,sh} = 4.5$ mm. The material constituting the magnets presents a Curie temperature of 310 °C. Rotor laminations are made from NO20-1200H electrical steel.

The power converter features a multilevel switching cell array architecture [2], including six main boards or legs, one for each phase. Each converter leg is composed of 8 Switching Cells (SCs) and 12 capacitors. The switching includes a main power switch and its driver, along with the iFuse. The electric motor and converter legs are integrated by a shared water-cooled case that features a hexagonal shape with the external walls serving as cold plates for the converter legs. The cooling channels present a simple helical design with a height of 5 mm and a width of 40 mm. Figure 1 reports the schematic of the proposed integrated assembly, which is based on a hexagonal case housing the motor, with the external flat surfaces serving as cold plates for the converter legs.



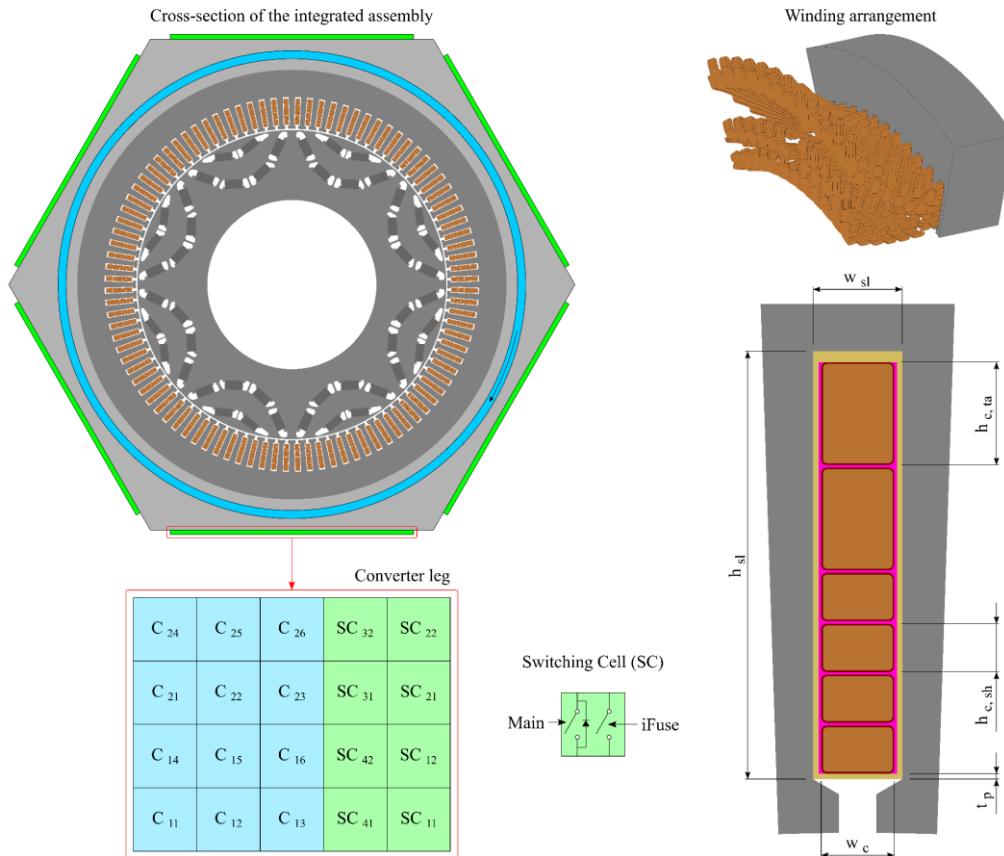


Figure 1 – Schematic representing the integrated assembly composed by the electric motor and the IIC.

2.2. Numerical methods

The integrated assembly composed of the electric motor, the power converter, and their shared cooling system is modelled by means of Lumped Parameter Thermal Networks, which are often referred to as LPTNs. Three LPTNs with varying number of degrees of freedom are developed with the aim of evaluating the effect of modelling complexity on numerical results, specifically on the estimation of hot-spot temperatures. The development of the lumped parameter thermal networks is presented in the following.

2.2.1. Two-dimensional thermal model

The physical domain of the electric motor is reduced to a geometry consisting of a single slot, along with the associated conductors and insulation, and half of the two adjacent teeth. Figure 2 shows a schematic of the 2D LPTN. The conductive thermal resistance between a pair of nodes is evaluated by summing the contributions given by each layer of material:

Equation 1

$$R_{cond} = \sum_j \frac{1}{S_j \lambda_j}$$

Where S_j and λ_j are the conduction shape factor and the thermal conductivity of each layer of material j , associated with the considered heat flow path. The shape factors for flat, radial, and circumferential flow path are given by:

Equation 2



$$S_{fp} = \frac{A}{t}, \quad S_r = \frac{\Delta z \Delta \varphi}{\ln\left(\frac{r_{ext}}{r_{int}}\right)}, \quad S_\varphi = \frac{\Delta z \ln\left(\frac{r_{ext}}{r_{int}}\right)}{\Delta \varphi}.$$

The values of thermal conductivity considered for all the materials making up the electric motor are listed in Table 1. The contact resistances between the stator and the internal wall of the cooling jacket are estimated by modelling heat transfer between the two uneven surfaces as heat conduction through an equivalent layer of still air. The associated thermal resistances are computed by considering a flat-plate shape factor:

Equation 3

$$R_{co} = \frac{t_{eq}}{\Delta \varphi r_{s,ext} l_{ss} \lambda_{air}}$$

where t_{eq} is the thickness of the equivalent layer of air between the stator and case. t_{eq} is set to 0.006 mm, as it representative of a coupling between iron and aluminium components with loose tolerances [3], which is a conservative assumption from the point of view of thermal management. The convective resistances in the air gap and cooling jacket are defined as follows:

Equation 4

$$R_{conv} = \frac{1}{U A},$$

Component	Material	λ [W m-1 K-1]
Stator and rotor laminations	NO20-1200H electrical steel	21.0
Winding conductors	Copper	385.0
Wire enamel	Voltatex®	0.23
Impregnation resin	SbTCM resin	3.20
Insulating paper	Kapton®	0.12
Magnets	N40UH NdFeB	6.45
Shaft	Steel	45.0
Case	Aluminium	237.0
Thermal pad	Carbon fibre	20.0

Table 1 - Values of thermal conductivity of the materials associated with the main components of the electric motor.

where U is the convective heat transfer coefficient. In the air gap, U-values are obtained from the correlation by Bjorklund and Kays [4] for Taylor-Couette flows:

Equation 5

$$Nu = \frac{U D_h}{\lambda} = 0.35 Ta^{0.25},$$



where Ta is the Taylor number, which is computed based on the angular velocity of the rotor ω , its radius $r_{r,ext}$ and the height of the air gap h_{ag} :

Equation 6

$$Ta = \frac{\omega^2 r_{r,ext} h_{ag}^3}{\nu^2}$$

The Heat Transfer Coefficients (HTCs) associated with the cooling jacket are derived from the CFD model presented in Section 2.2.7. The heat generated by a single conductor of length l_c and cross-sectional area A_c is modelled as follows [5]:

Equation 7

$$\dot{Q}_c = \gamma_{cu} \frac{l_c}{A_c} I^2 \left[\frac{K_{rk} - 1}{\sqrt{1 + \alpha_{cu}(T - T_{ref,cu})}} + 1 + \alpha_{cu}(T - T_{ref,cu}) \right],$$

where γ_{cu} is the electrical resistivity of copper, which is evaluated at the reference temperature $T_{ref,cu} = 20 \text{ }^\circ\text{C}$: $\gamma_{cu} = 1.724 \times 10^{-8} \text{ } \Omega\text{m}$. α_{cu} is the temperature coefficient of copper, which equates to $4.29 \times 10^{-3} \text{ }^\circ\text{C}^{-1}$. The K_{rk} -values are derived from 2D Finite Element Analyses analogous to those presented in [6] and [7], which are also used for the losses associated with the laminations of the yoke, the teeth, the rotor, and the magnets (Table 2). In this case, temperature effects are not considered as they are much less relevant compared to those in the copper windings.

Component	Yoke	Teeth	Rotor	Magnets
Losses [W]	1028.5	848.7	290.0	7.952

Table 2 – Losses produced by the stator and rotor laminations, and permanent magnets.

The thermal model of the rotor is developed by simplifying the actual geometry of the rotor to represent it in a cylindrical reference frame at a reduced node count. The conduction thermal resistances are obtained from Equation 1 using the radial and circumferential shape factors in Equation 2.

In the thermal model of the power converter, the nodes standing for the main and iFuse switches are connected in parallel to the last copper layer of the PCB through $R_j = 0.62 \text{ }^\circ\text{C/W}$, which models heat conduction between the junction of the semiconductors and the last copper layer of the PCB. The latter is connected to the case by means of a conductive carbon fibre thermal pad that has a thickness of $t_{pad} = 0.4 \text{ mm}$. The convective resistance between the cooling fluid and the external wall of the case is obtained from the CFD model presented in Section 2.2.7. The switching and conduction losses of each power device are derived by using the approach presented in [8], and by considering the reference temperature $T_{ref,j} = 100 \text{ }^\circ\text{C}$. These losses are listed in Table 3, where values in red refer to conduction losses in iFuses, occurring when these devices are made out of the same semiconductors used for the main switches, which are optimized for switching performance. On the other hand, values in green are referred to a power switch optimized for



continuous conduction. In this case, the losses of each switching cell are computed considering the non-optimal configuration as it is more demanding from the thermal point of view.

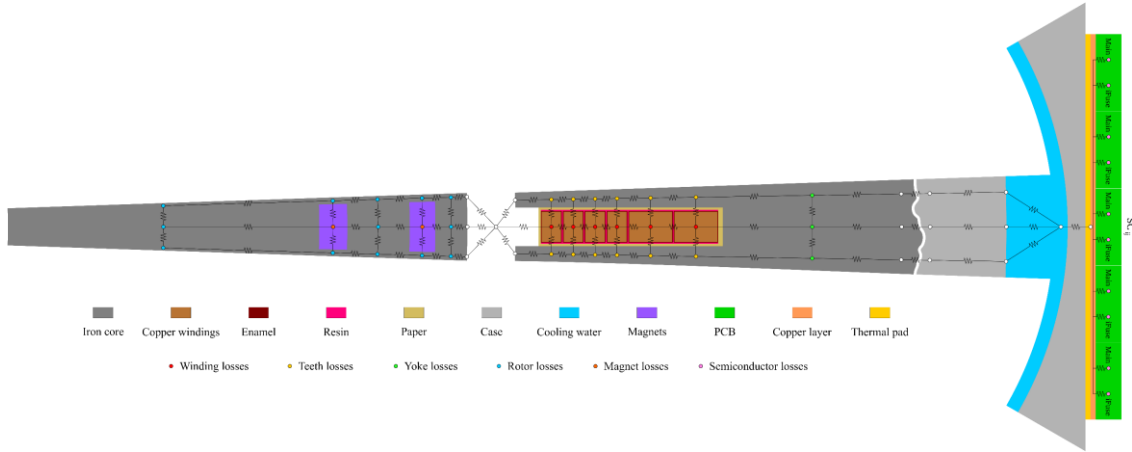


Figure 2 – Arrangement of nodes and thermal resistances constituting the two-dimensional thermal model of the electric motor integrated with the IIC.

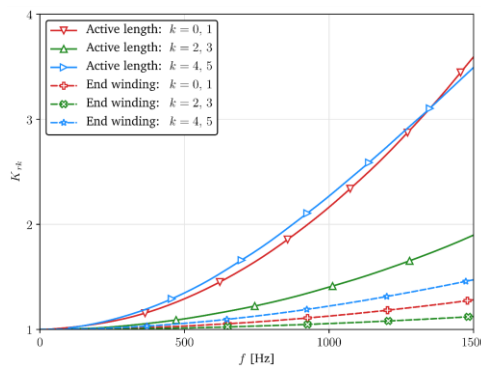


Figure 3 – Values of AC/DC loss ratios K_{rk} as a function of frequency for all conductor layers in the active section of the motor, and in the end-windings.

Conduction losses in Table 3 are scaled with the junction temperature of the semiconductors according to the following relation from WP3 [1]:

Equation 8

$$Q_{SC-co} = Q_{SC-co}(T = T_{ref,SC})[1 + 1.429 \times 10^{-3}(T - T_{ref,SC})].$$



Switching cell	Sub-component	P_{cond} [W]	P_{sw} [W]	P_{tot} [W]
SC11, SC12, SC41, SC42	Q1 (main)	9	43	52
	Q2 (iFuse)	9	0	9
SC21, SC31	Q1	7	21	28
	Q2	7	0	7
SC22, SC32	Q1	41	0	41
	Q2	41	0	41

Table 3 – Values of conduction, switching, and overall losses associated with each SC.

2.2.2. 3D single-slot thermal model

The two-dimensional thermal model is extended along the axis of the motor to derive a primitive 3D LPTN encompassing a single slot of the electric machine and a single converter leg. The arrangement of nodes and resistances constituting the thermal models of the stator and rotor is replicated three times, subdividing the domain into three axial slices, as shown in Figure 4. The nodes that identify a subregion of the model, namely all centre-point nodes, are connected by axial resistances that are defined as in Equation 2. The end windings are modelled by considering six open-ended conductors on either side of the active section of the motor. The end winding losses are evaluated by means of Equation 7, using the K_{rk} coefficients in Figure 3 [9]. The lateral surfaces of the end windings are assumed adiabatic, as this represents the most unfavorable scenario for thermal performance. The advection of thermal energy due to coolant flow in the case is modelled by advective resistances defined as

Equation 9

$$R_{adv} = \frac{\Delta T}{\dot{Q}} = \frac{T_{b,o} - T_{b,i}}{\dot{m} c_p (T_{b,o} - T_{b,i})} = \frac{1}{\dot{m} c_p}$$

The LPTN presented in Figure 4 is used to model the complete integrated motor drive by using the parallel rule:

Equation 10

$$R_{ij, full} = \frac{R_{ij}}{n_{par}}, \quad \dot{Q}_{i, full} = \dot{Q}_i n_{par},$$

where n_{par} is equal to the number of slots (96) for all resistances and losses associated with the motor, while it is equal to 6 for the resistances and losses associated with the power converter. These assumptions allow for a correct evaluation of the coolant temperature increase at a reduced node count, as the losses of the complete assembly are injected into a simplified model.



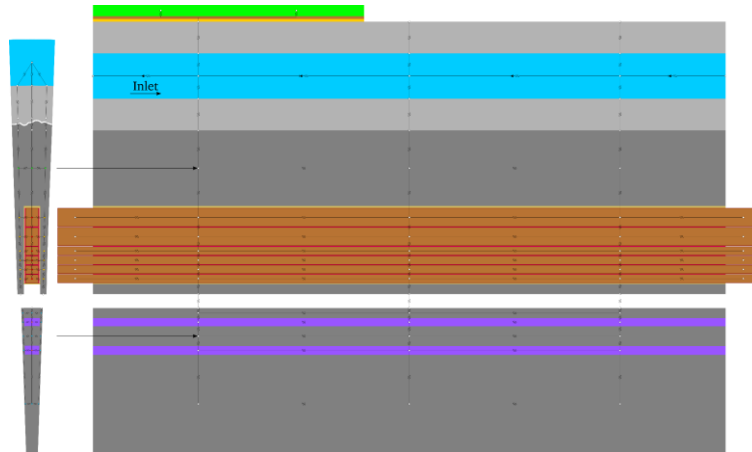


Figure 4 - Longitudinal section of the 3D LPTN of a single slot positioned at the centerline of the windings.

2.2.3. Complete 3D thermal model

The complete three-dimensional model of the integrated motor drive is obtained by starting from the 2D LPTN and reproducing its arrangement of nodes and resistances 96 times along the circumferential direction and three times along the axial one. All interior nodes are connected by circumferential and axial resistances defined based on their respective conduction shape factors. By modelling the complete motor, the connections between the winding layers can be accurately represented. The thermal connections are arranged as the electrical connections, as shown in Figure 5. The coolant temperature nodes associated with the slots are connected by advective resistances and thermal diodes following the path of coolant within the case, as shown in Figure 6. Figure 7 reports a schematic of the front face of the complete 3D thermal model.

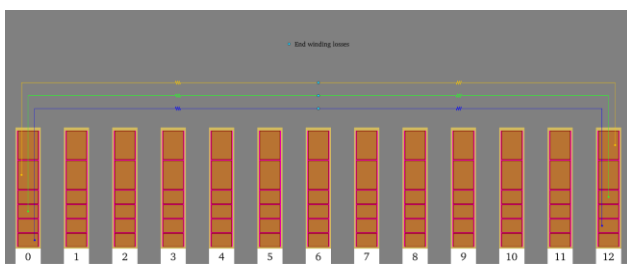


Figure 5 - Thermal connections between winding layers.

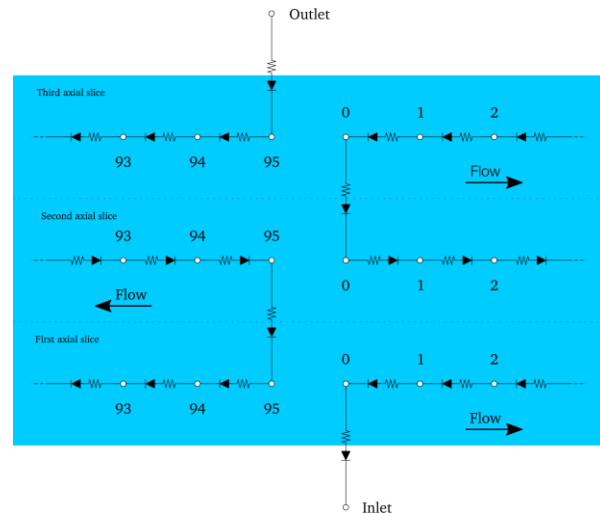


Figure 6 - Thermal connections between coolant nodes.



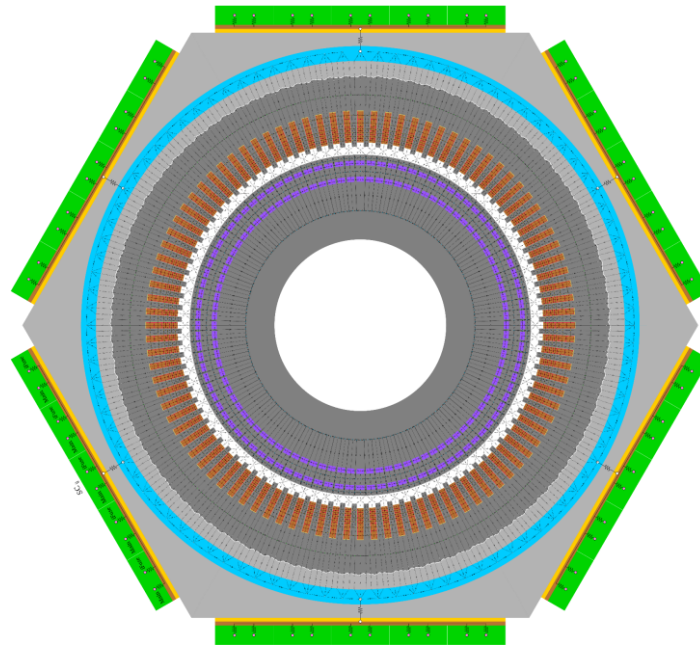


Figure 7 - Schematic showing the front face of the complete three-dimensional thermal Model of the integrated motor and converter assembly.

2.2.4. Boundary conditions and implementation

The boundary conditions applied to the thermal models are summarized in Table 4. The lumped parameter thermal networks are implemented in Python 3 using in-house library MuSA

2.2.5. Validation of advective thermal resistances and thermal diodes

The correct implementation of the advective resistances included in both the 3D LPTNs presented in Section 2.2.2 and Section 2.2.3 is verified by comparing numerical results on the coolant bulk temperature increase with the expected ΔT_b -value retrieved from:

Equation 11

$$\Delta T_b = \frac{Q_{tot}}{\dot{m} c_p},$$

where Q_{tot} is the sum of all losses introduced in the model. Table 5 reports the expected values of ΔT_b , their numerical counterparts, and the difference between them. Negligible deviations between the two sets of results are noted.

Parameter	Value	Units
Phase current	80	A
Rotor speed	9000	rpm
Phase frequency	600	Hz
Coolant flow rate	5	l/min
Mean coolant temperature – 2D model	68.6	°C
Inlet coolant temperature	60	°C

Table 4 - Boundary conditions applied to the thermal models developed for the integrated assembly under examination.



2.2.6. Validation of the 2D motor thermal model

The thermal modelling approach developed in this work is validated by comparing numerical results from the two-dimensional thermal model with those derived from a Finite Element Analysis performed on the same motor geometry, which is presented in [7]. Figure 8 shows the comparison between the temperature values obtained from the 2D LPTN and FE models in the windings and in the stator magnetic circuit, showing a very good agreement between the two models.

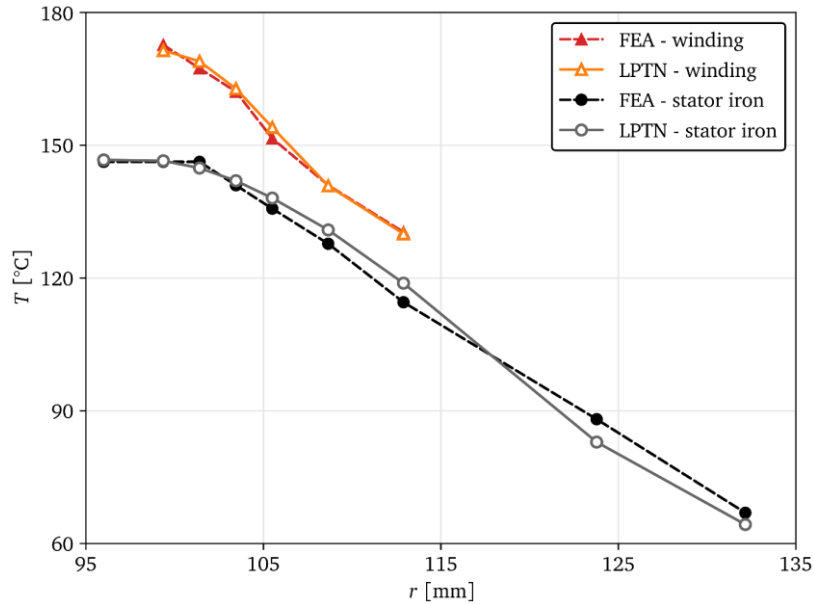


Figure 8 - Comparison between the temperature values of the windings and stator iron obtained from the LPTN and FE models

Model	Expected ΔT_b	Model ΔT_b	Deviation
3D single-slot model	17.25	17.25	1.7×10^{-13}
Complete 3D model	17.25	17.25	4.7×10^{-11}

Table 5 - Expected and numerical values of bulk temperature difference obtained from the two three-dimensional thermal models. Values in °C.

2.2.7. Numerical model of the cooling jacket

The HTC's associated with the internal and external walls of the cooling jacket are obtained by developing a dedicated CFD model, comprising a sixth of a single channel under periodic conditions. The flow is governed by the RANS and energy equations:

Equation 12

$$\begin{cases} \nabla \cdot (\vec{v} \otimes \vec{v}) = -\frac{1}{\rho} \nabla p + \nabla \cdot [(\nu + \nu_t) \nabla \vec{v}] + \sigma \\ \nabla \cdot \vec{v} = 0 \\ \nabla \cdot (\rho \vec{v} h) + \nabla \cdot \left(\rho \vec{v} \frac{|\vec{v}|^2}{2} \right) = -\nabla \cdot \vec{q} + \nabla \cdot (\vec{\tau} \cdot \vec{v}) \end{cases}$$

Temperature in the aluminium walls is determined as follows:

Equation 13

$$\nabla^2 \cdot T = 0$$

The $k-\omega$ SST turbulence model [10] is employed to compute eddy viscosity. The momentum source term σ in Equation 12 stands for the external forcing needed to maintain the desired flow rate.

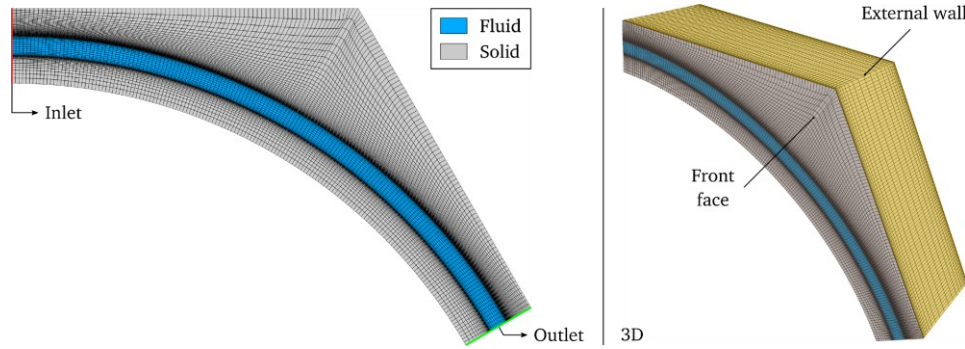


Figure 9- Selected views of the computational mesh of the CFD model developed for the cooling jacket.

A fully developed flow solution is attained by enforcing periodic boundary conditions between the inlet and outlet patches for all fields. No slip conditions are applied at the front and back faces of the domain, as well as at the fluid–solid interface, where the continuity of temperature and heat fluxes is also enforced. The two HTC’s are obtained by imposing and entering heat flux to the considered wall and setting the other as adiabatic. This procedure is repeated for the internal and the external walls, the latter serving as the cold plate for the converter legs. The numerical solution is obtained by using the SIMPLE algorithm [11] implemented in the OpenFOAM computational suite [12]. Advective terms are discretised by means of second-order upwind schemes. Instead, central schemes featuring explicit non orthogonality correction are used for diffusive terms. Figure 9 shows the selected views of the computational grid.

The influence of the grid on numerical results is assessed by developing three computational meshes with different cell sizes, and comparing the numerical results obtained. These are listed in Table 6, along with the average size of the cells Δ^* , the integral mean values of the dimensionless wall distance \bar{y}^+ , and the value of the Nusselt number associated with the internal wall Nu_{int} obtained at zero grid spacing by means of Richardson’s extrapolation [13]. Numerical results do not show a convergent behavior with respect to the mean element size. However, numerical results from the coarse grid may not be reliable as \bar{y}^+ is well above unity, which is considered the upper limit for the use of low-Reynolds turbulence models. The fine grid produces results close to the extrapolated continuum value. For these reasons, results from the fine grid are considered for all subsequent thermal analyses.

	Δ^*	\bar{y}^+	Nu_{int}	Deviation
Coarse grid	0.1	4.7	24.9	-
Medium grid	0.05	0.72	21.2	-14.9%
Fine grid	0.025	0.37	22.4	+5.6%
Richardson’s extrapolation	-	-	22.8	+1.7%

Table 6 – Numerical results from the mesh sensitivity analysis and from Richardson’s extrapolation.

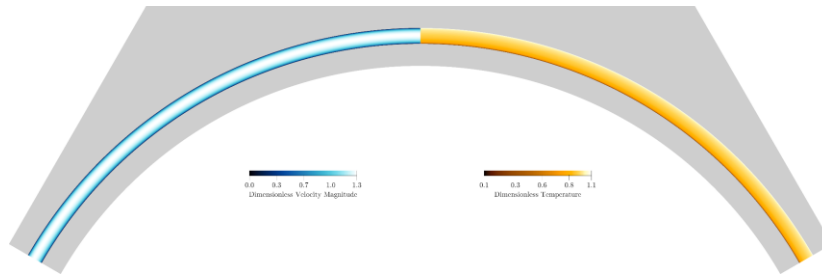


Figure 10 - Colourmaps of dimensionless velocity magnitude and temperature difference on a transversal cross-section of the cooling jacket.

2.3. Results

Figure 10 shows colourmaps of dimensionless velocity magnitude and temperature difference $\Delta T^* = (\bar{T}_{wall} - T)/(\bar{T}_{wall} - \bar{T}_b)$, obtained on centered transversal sections of the cooling jacket. As expected, the velocity profile is not symmetric with respect to the channel centerline due to centrifugal forces. The HTC's related to the internal and external walls are expressed as follows

Equation 14

$$Nu = \frac{q''y}{\lambda(\bar{T}_{wall} - \bar{T}_b)},$$

In the case of a flow of a 50% by mass solution of water and ethylene glycol at 5 l/min, the Nusselt number values related to the inner and outer walls are 22.4 and 17.4, respectively.

Table 7 reports the hot-spot temperatures in the windings, SCs and magnets. In all cases, the maximum temperatures are well below the theoretical limits of each component. Figure 11 presents the distributions of temperature and heat fluxes in the stator of the electric motor, obtained from the 2D model. As expected, the winding temperature hot-spot is located at the winding layer closest to the rotor, as it presents the largest equivalent thermal resistance to the cooling system.

On average, the T_{max} -values derived from the 2D LPTN are lower than their counterparts from the 3D models, as the 2D model does not include losses in the end windings. The temperature values associated with the power converter are the least sensitive to the type of approach, as the converter board are placed towards the front of the motor where the coolant inlet is located. The two 3D approaches show comparatively similar results, confirming the validity of the use of the parallel rule for the extension of the single-slot 3D model. Figure 12 shows the temperature distributions of all six winding layers along the axial direction, which is denoted by z . In the case of the complete 3D LPTN this distribution is obtained by averaging winding temperatures along the circumferential direction, to make a fair comparison with the outcomes of the single-slot 3D approach. Figure 13 reports a contour plot of the temperature distribution of stator and rotor on a transversal cross-section at the centerline of the motor. The effects of the increasing coolant temperature along the circumferential direction does not produce relevant temperature gradients. The 3D single-slot includes a much smaller number of nodes and thermal resistances, which greatly reduces computational and development times. For this reason, this model is deemed to be the best compromise between practicality and accuracy.



Model	Component	Temperature limit [°C]	T_{max} [°C]	$T_{max} - T_{ref}$ [°C]	Computational time [s]
2D	Windings	180	115	46	0.08
	Magnets	310	183	114	
	Converter	200	115	46	
3D single slot	Windings	180	129	69	0.26
	Magnets	310	192	132	
	Converter	200	118	58	
3D complete	Windings	180	127	67	51.7
	Magnets	310	189	129	
	Converter	200	118	58	

Table 7 – Hot-spot temperature results associated with the main components of the assembly, and obtained from the three lumped parameters thermal models.

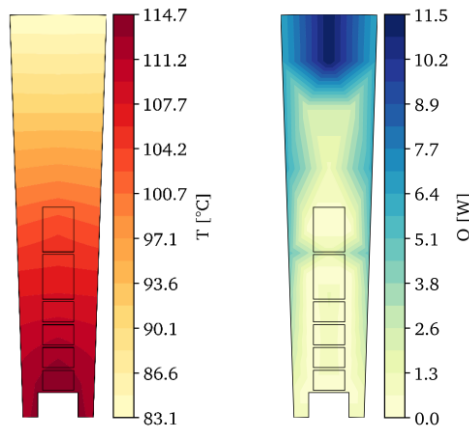


Figure 11 – Distributions of temperature and heat fluxes in the stator of the electric machine, obtained from the two-dimensional thermal model of the integrated assembly.

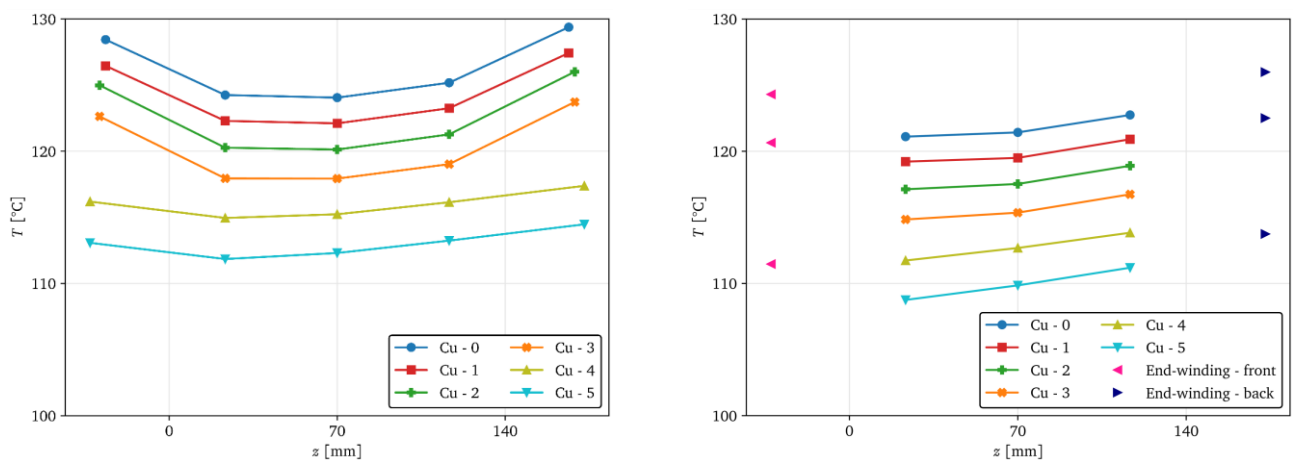


Figure 12 – Distributions of winding temperatures along axis of the motor, obtained from the 3D single-slot model (left) and complete 3D LPTN (right)



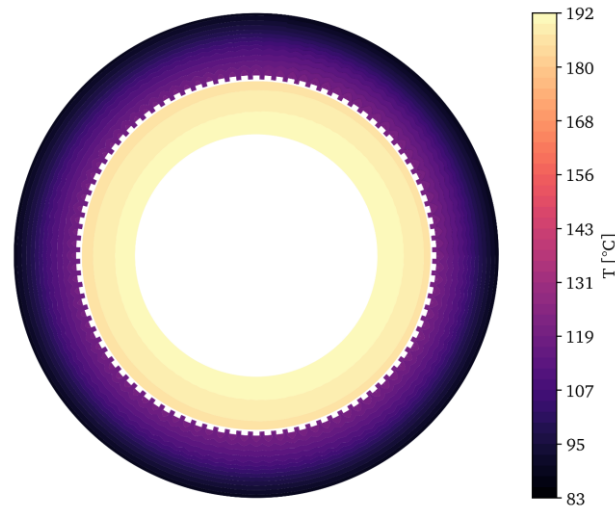


Figure 13 - Temperature contour plot of the stator and rotor obtained on a cross-section located at the center of the motor, considering numerical results from the complete 3D thermal model.

2.3.1. Parameter sensitivity analysis

The 3D single-slot model is employed to evaluate possible improvements to the thermal performance of the integrated assembly, by performing a comprehensive parameter sensitivity analysis. Specifically, several simulations were carried out by changing each time the thermal conductivity of one of the constitutive materials by considering commercially available variants that perform the same functions. In addition, the values of the convective thermal resistances and the thermal resistance between the junction and the last copper layer of SCs were varied considering a $\pm 25\%$ deviation, which represents a reasonable estimation error that is usually associated with the use of empirical and numerical models. Table 8 reports the values of the thermal properties and associated deviations with respect to the baseline parameters.



Component	Value	Materials	Limits	Deviations
Conductors	λ_c	Copper, T=0 °C	404	+0.6%
		Copper, T=180 °C	389	-3.0%
Enamel	λ_e	Kapton CR + NP1025 [14]	0.419	+82.2%
		Magnetemp CA 200 [14]	0.114	-50.4%
Resin	λ_{rs}	EpoxyLite [15]	0.85	-73.4%
		Varnish [15]	0.25	-92.2%
Paper	λ_p	DMD [16]	0.2	+66.7%
		TVAR [16]	0.116	-3.3%
Iron core	λ_{cr}	50A1300 [17]	63.1	+200%
		50A230 [17]	17.9	-14.8%
Magnets	λ_m	SmCo [18]	12.0	+85.9%
		NdFeB [18]	2.0	-69.0%
Thermal pad	λ_{pad}	Dielectric pad	6.5	-67.5%
		Dielectric pad	2.0	-90.0%
Air gap	U_{ag}		137	+25.0%
			87.9	-25.0%
Power converter	R_j		0.78	+25.0%
			0.5	-25.0%
Cooling jacket	U_{int}		2385	+25.0%
			1526	-25.0%
	U_{ext}		1849	+25.0%
			1184	-25.0%
Stator-case interface	R_{co}		0.426	+7.17%
			0.04	-90.0%

Table 8 - Values of thermal conductivity of the materials associated with the main components of the electric motor and power converter. Values of λ in W/(mK), values of U in W/(m² K), and values of R in °C/W

Temperature results were presented by a relative temperature difference:

Equation 15

$$\vartheta = \frac{T - T_b}{(T - T_b)_{bsl}}$$

where T_b is the imposed inlet coolant bulk temperature and the subscript bsl refers to the baseline set of parameters. Figure 14 shows contour plots of ϑ from the sensitivity analyses performed on the parameters associated with the stator of the motor. Despite the broad temperature range considered for the computation of λ_c , negligible effects are observed on the temperature outcomes. The different choice of insulating material for the lining of the conductors causes moderate ϑ deviations of +4%/-3%, which are concentrated in the vicinity of the first winding layer, i.e. the hot-spot. Thus, selecting a wire coating with improved thermal properties could provide slight performance benefits in terms of power output. The change of the impregnation resin appears to have similar effects to those observed for the wire enamel. Insulating paper with a greater λ -value provides a moderate improvement to the thermal performance of the stator and



winding assembly. However, these are concentrated at the last winding layer, while noticeably higher ϑ -values are noted in correspondence of the first layer (hot-spot). Thus, minor improvements in power output should be expected. The thermal model shows a marked sensitivity to the thermal conductivity of the iron, as it constitutes most of the stator and rotor of the machine. However, it is important to stress that any temperature change observed due to the change of λ_{cr} may be offset by the core losses, which might vary substantially with different choices of materials for the core. As expected, both the convective resistances associated with the cooling jacket and the contact resistances have a marked effect on the temperature, particularly close to surface of the stator, while less marked effects are noted with increasing distance from the surface, as the relative contributions given by the convective and contact resistances to the equivalent resistance between a given point and the cooling fluid decrease in favor of those given by conductive resistances. Figure 15 shows the results obtained for the rotor. Compared to the stator, the rotor presents more uniform ϑ distributions. The thermal conductivity of the core and the heat transfer coefficient in the air gap are clearly the most influential parameters for the thermal performance of the rotor. The ϑ -values obtained for the power converter are shown in Figure 16. All the parameters have substantial effects on the temperature field, as the thermal model of the power converter includes a lower amount of parameters compared to the other two LPTNs.



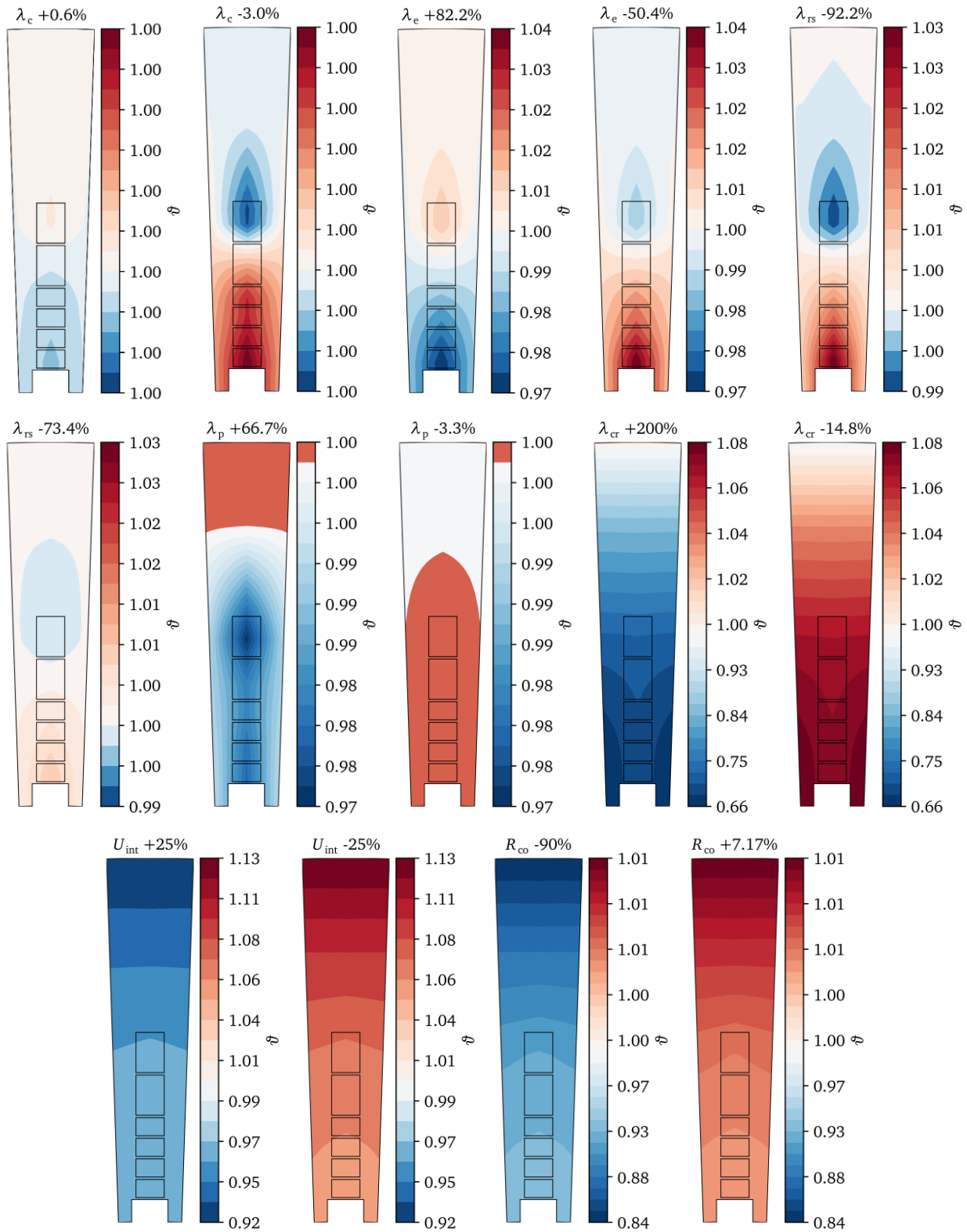


Figure 14 - Contour plots of dimensionless temperature difference on the stator, obtained from the sensitivity analyses performed on the most relevant constitutive parameters associated with the stator of the motor.



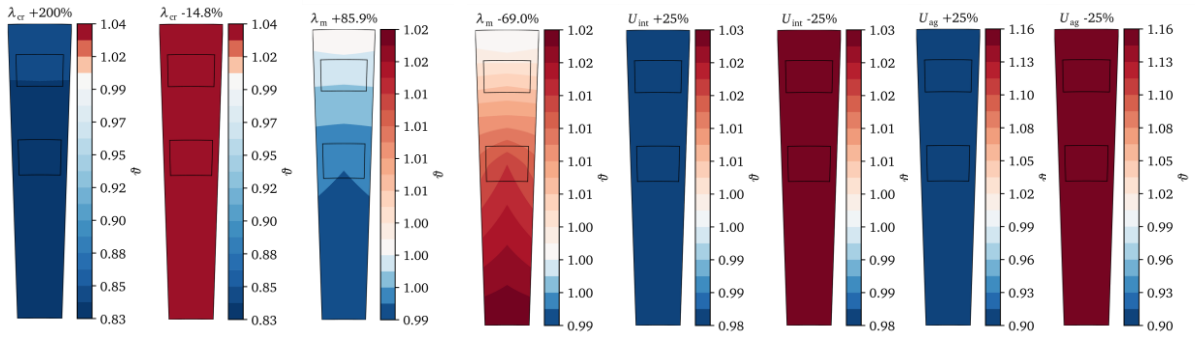


Figure 15 – Contour plots of dimensionless temperature difference on the rotor, obtained from the sensitivity analyses performed on the most relevant constitutive parameters associated with the rotor of the motor.

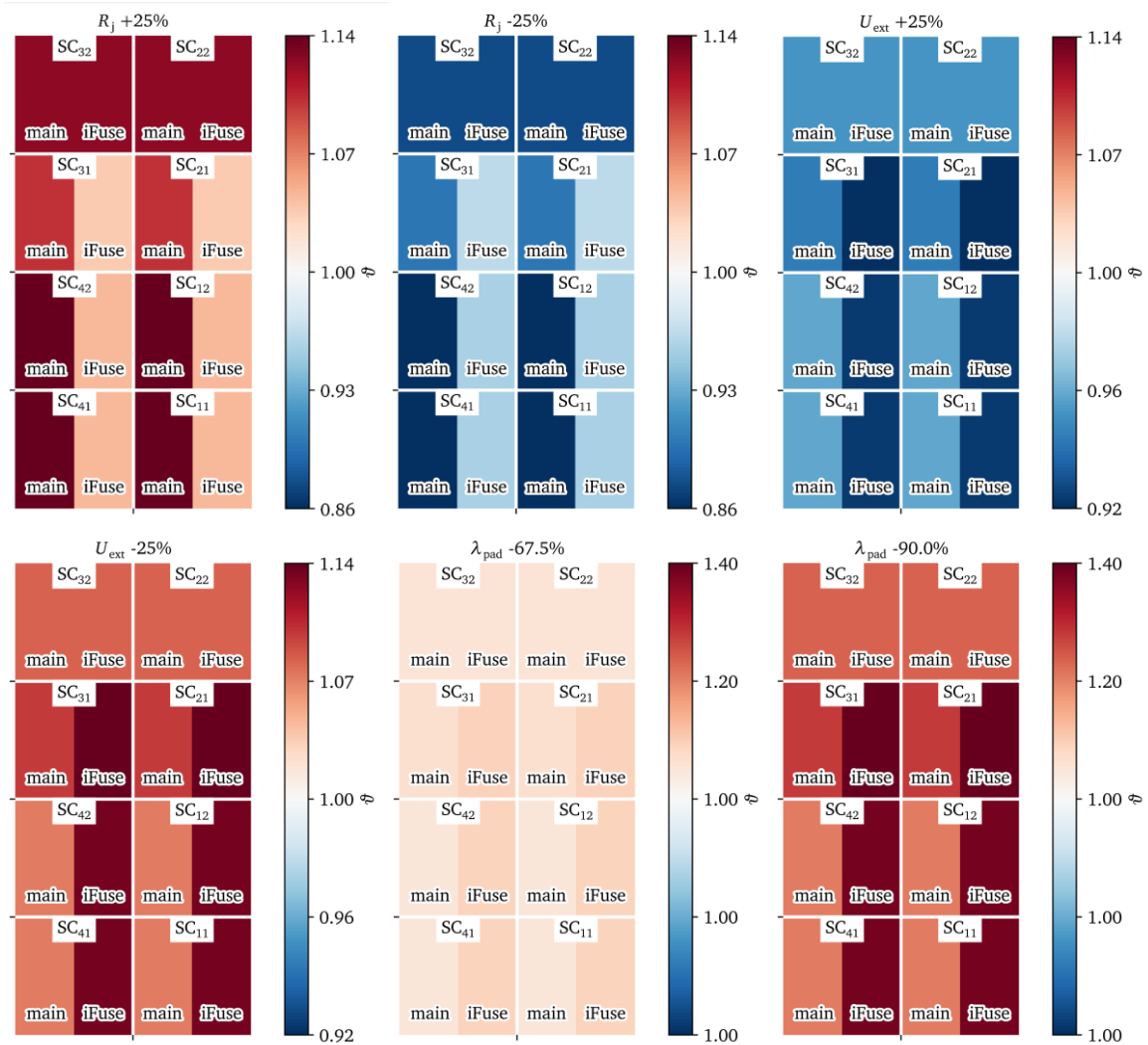


Figure 16 – Contour plots of dimensionless temperature difference on the power converter, obtained from the sensitivity analyses performed on the most relevant constitutive parameters associated with power converter.

3. BIC Integration

The energy storage system examined in this work includes 2 battery packs rated at 50 kWh each one. The two packs are configured in series, with the first connected to the BIC (a ML-DAB DC-DC converter). Each battery pack comprises 248 modules arranged in an 8S31P configuration and each module comprises 26 cells arranged in a 13S2P configuration. Table 9 summarizes the configuration and specifications of the battery packs. The LV side of the power converter comprises 2 legs, each with 10 SCs; the HV side also comprises 2 legs, each with 4 SCs. The SCs and the HF transformer are cooled by the same cooling plate that manages the battery temperature. Figure 17 shows the system layout. The cooling channels are 2 parallel serpentine. Figure 18 shows one of the four plate coolers and cell stack forming the integrated battery pack and BIC power converter. The batteries are in contact with the top surface of the plate, while the BIC is in contact with the bottom surface. The BIC is positioned near the inlet of the second channel to take advantage of the coolant's minimum temperature. The coolant is a 50% mixture of ethylene glycol and water. The channels have a 35 mm x 5 mm rectangular cross-section .

Cell data	
Type	ICR18650-22P
Chemistry	LiNiMnCoO2
Cell diameter [mm]	18.0
Cell height [mm]	65.0
Cell capacity [Ah]	2.15
Cell nom. voltage [V]	3.60
Module data	
N° cell series	13
N° cell parallels	2
Module capacity [Ah]	4.30
Module nom. voltage [V]	46.80
Pack data	
N° module series	8
N° module parallels	31
Module capacity [Ah]	133.30
Pack nom. voltage [V]	374.40

Table 9 - Battery pack data

3.1. LPTN model

To model the batteries-BIC system a LPTN was created and solved with *MUSA*. Each module is represented by a node connected to the busbar node with a contact thermal resistance. This is then followed by a conductive thermal resistance, which represents the thermal pad layer between the busbar and the top surface of the plate (see Figure 19). The coolant nodes are connected to the top surface of the plate via convective resistances and the connection between two adjacent fluid nodes is defined by advective resistances Equation 9).



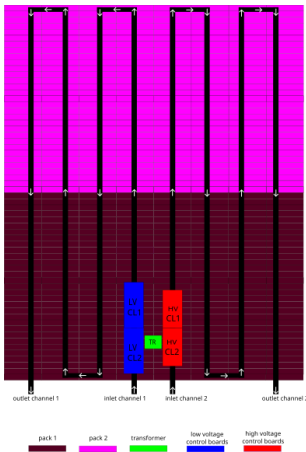


Figure 17 – Scheme of the cooling channels

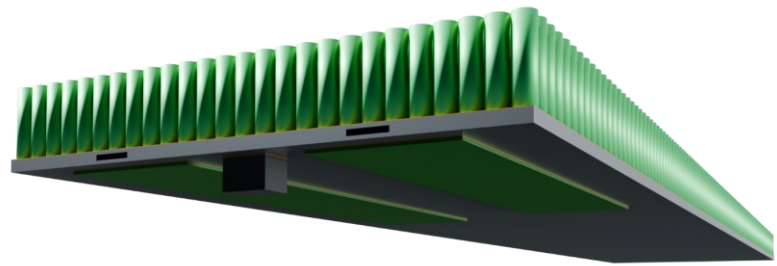


Figure 18 – Three-dimensional view of one of the four plate coolers and cell stack forming the integrated battery pack and BIC power converter, whose components are mounted on the bottom of the plate cooler.

It is assumed that the temperature at the battery terminals is the same as at the battery centre, as the thermal conductivity of batteries in the axial direction is usually two orders of magnitude higher than in the radial direction. Figure 20a shows the thermal network of a single LV leg, where each SC is represented by a node connected to the copper layer node through the junction thermal resistance, followed by a conductive resistance modelling the conductive pad. The same philosophy is applied to modelling the HV leg (Figure 20b). The transformer network (Figure 20c) includes the winding and core nodes linked by the winding-core thermal resistance. The core node is then connected to the external surface of the transformer via conductive resistance. The transformer surface node is connected to the bottom surface of the plate through the thermal pad resistance. Conductive resistances are evaluated as in Equation 1, convective resistances are evaluated using Equation 4 where the convective heat transfer coefficient, together with the friction factor, is determined by means of a CFD simulation of a periodic channel module, using the same methodology as described in Section 2.2.7. The heat of the BIC come from experimental measurements, and they are 5.22 W for a single LV leg, 9.5 W for a single HV leg and 8.6 W for the transformer. The BIC configuration is specified in [1]. Figure 21 shows the heat losses for each cell of the LV leg, while on the HV side the heat dissipated is uniformly distributed between the SCs. Finally, the winding and core in the transformer dissipate 6.3 W and 2.3 W respectively.

The electro-thermal model of the battery modules is based on a 3rd order Thevenin model to evaluate the voltage losses, and on the Bernardi's equation [20] for modelling the heat generated inside the batteries. The first term in Bernardi's equation represents heat generated by the Joule effect, while the second term represents reversible heat due to changes in entropy during chemical reactions. The data needed to develop the Thevenin model was obtained by experimental tests from UPC in 2017 with a custom-made module manufactured by the company *Bikelec*. The entropy coefficient trend with state of charge (SOC) comes from a recent work that measured this coefficient using batteries with the same chemistry as those used in this study [21].

The simulation is unsteady, with a time step of 0.2 seconds and a simulated time of 1 hour. The network has 2516 nodes and 2516 branches, and the simulation takes 1.5 hours on an i7-2600 CPU



at 3.4 GHz. The input current comes from a WLTP drive cycle, shown in Figure 22. The splitting of the input current between the two battery packs is managed by a PI controller which aims to balance the SOC of the packs. In fact, Figure 23 shows that the C-rate is generally higher in pack 1, because it is connected to the BIC. Figure 24 shows the SOC of the two battery packs resulting from the simulation, confirming the effectiveness of the controller.

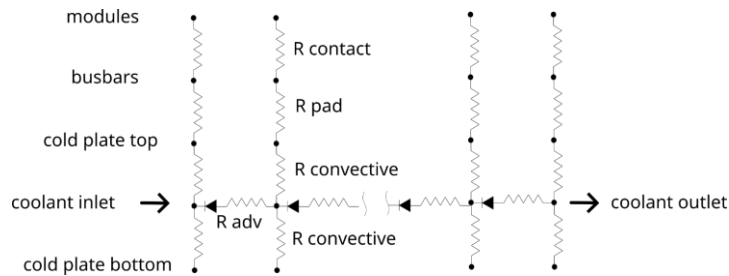


Figure 19 - Thermal network of the modules and cooling channels

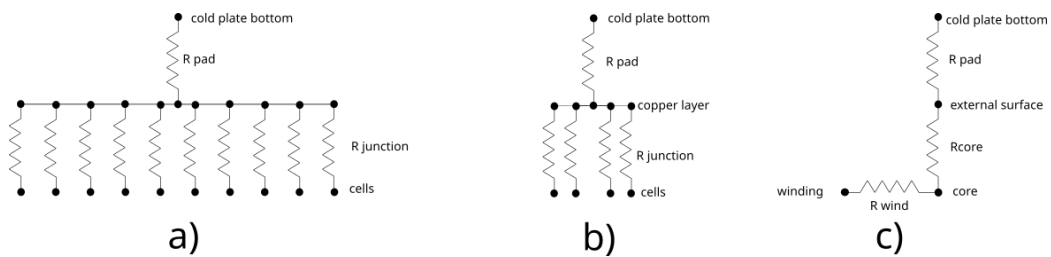


Figure 20 - Thermal network of a) LVSC single leg, b) HVSC single leg, c) transformer

SCp21: 0.39 W	SCp21: 0.39 W			
SCn22: 0.86 W			SCp11: 0.30 W	SCp11: 0.30 W
SCp12: 0.32 W			SCn21: 0.82 W	SCn21: 0.82 W
SCn11: 0.51 W	SCn11: 0.51 W			

Figure 21 - Losses of a single LV leg

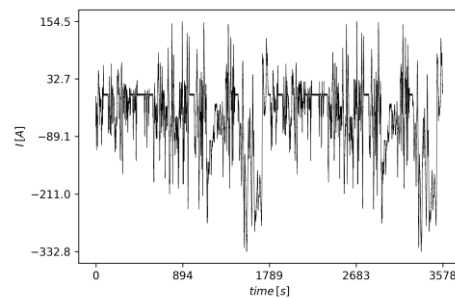


Figure 22 – Traction inverter current at its dc port for a WLTP driving cycle. A negative current indicates discharging of the battery

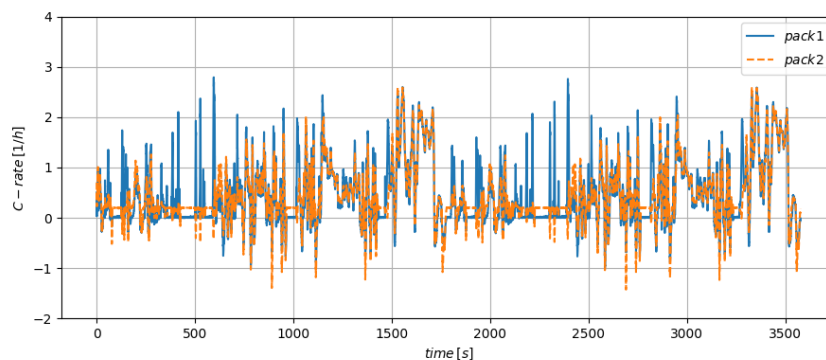


Figure 23 - C-rate profile

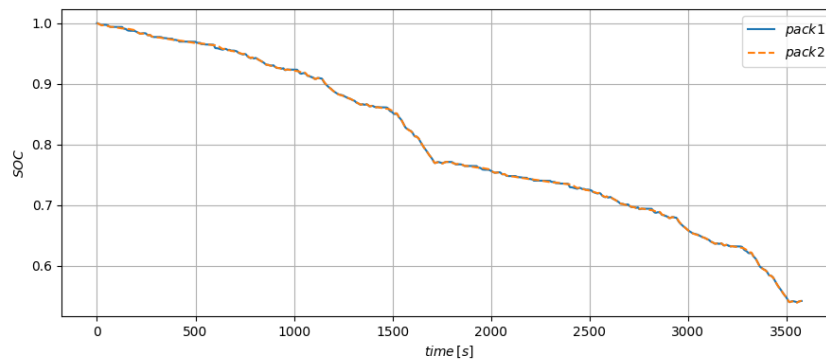


Figure 24 - SOC of the two packs

3.2. Results

The coolant flow rate in each serpentine is 20 l min^{-1} , and the mean Reynolds number is 3000. The convective thermal resistance from the CFD simulation 0.31 K W^{-1} . The coolant inlet temperature is $20 \text{ }^\circ\text{C}$. Figure 25 shows the temperature profile for the first and last modules of each pack, following the direction of the coolant flow. The temperature peaks in both plots occur at the same moments due to the higher current at these points. However, the maximum temperature is higher in the last modules because the coolant has already absorbed most of the heat generated inside the batteries. It can also be seen from the figure that the modules in pack 1 generally have a higher temperature than the modules in pack 2. This is because pack 1 receives a greater fraction of the input current, as it is also connected to the BIC. Figure 26 is a color map showing the maximum temperature at each point in the energy storage system. As expected, the minimum temperature occurs near the inlet of the channels, where the coolant is at its inlet temperature. The temperature then gradually increases as it flows towards the outlet. As shown in Figure 27, the presence of the BIC does not significantly influence the temperature distribution of the batteries. The modules thermally connected with the BIC have a temperature trend very similar to those of first modules in Figure 25, in fact the total heat dissipated from the HV and LV side is negligible with respect to the mean heat generated from the batteries. Figure 28 shows the temperature profile of the BIC components. Since the converter operates at a fixed power level, the temperatures remain almost constant throughout the simulation period. The maximum temperatures are $25.67 \text{ }^\circ\text{C}$ for the LVSCs, $29.38 \text{ }^\circ\text{C}$ for the HVSCs, and $105.05 \text{ }^\circ\text{C}$ and $99.06 \text{ }^\circ\text{C}$ for the transformer winding and core, respectively. It is worth mentioning that the thermal capacity of the BIC components was neglected as it can be considered negligible with respect to the thermal capacity of the batteries. The total pressure losses inside the channels are 0.61 bar, where 0.53 bar are the distributed losses and the remaining are the pressure losses because of the turns of the channels. From the results presented, all components are below their critical value, and the maximum temperature difference between the modules is on average $1.74 \text{ }^\circ\text{C}$ during the simulated timespan. The maximum value of the temperature difference, which is $6.34 \text{ }^\circ\text{C}$, occurs near the end of the simulation, where the plots present a peak of temperature. This parameter could be improved, as the maximum temperature difference should be kept below $5 \text{ }^\circ\text{C}$ in optimal operating conditions. To improve temperature uniformity, the flow rate can be increased (increasing the required pumping power) or new cooling channel layouts can be investigated.



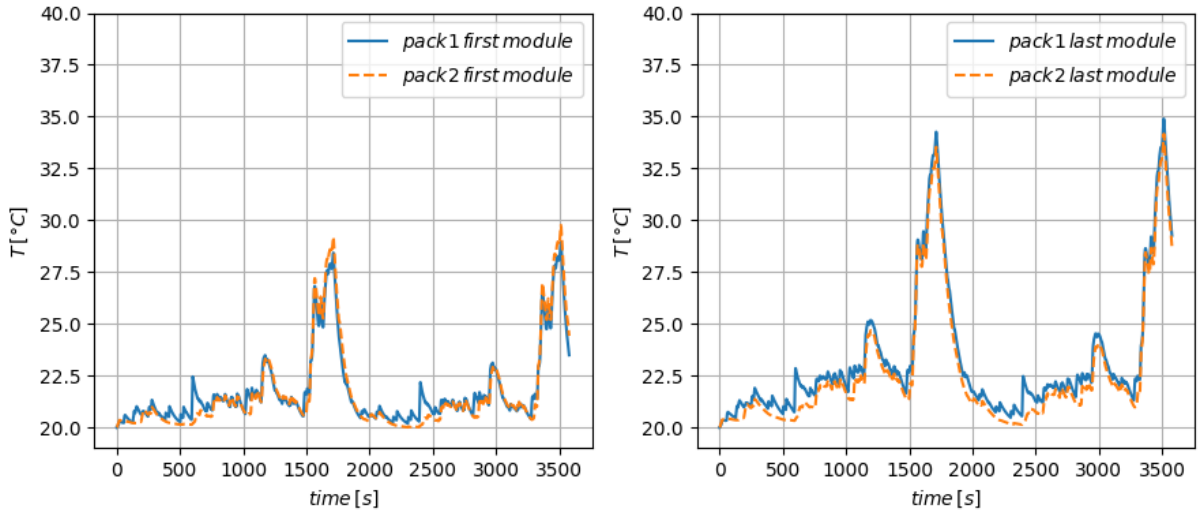


Figure 25 - Temperature profiles of the first and last module of each battery pack

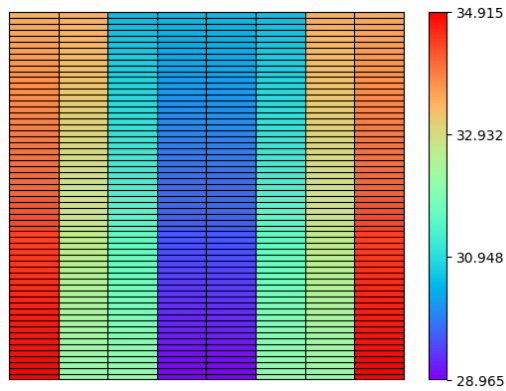


Figure 26 – Colormap showing the maximum temperature reached at each sector of the battery thermal model.

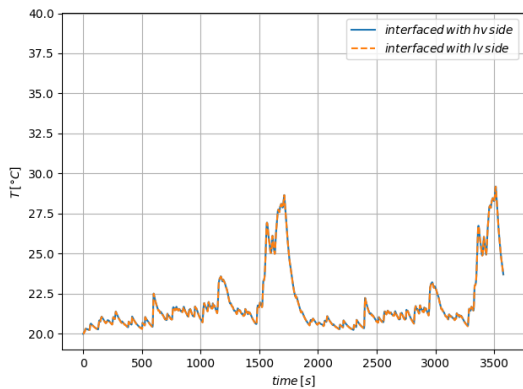


Figure 27 - Temperature of the battery modules underneath the high-voltage (HV) and low-voltage (LV) BIC boards.

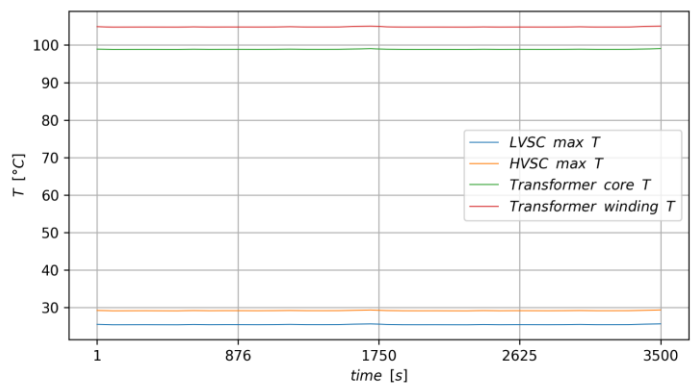


Figure 28 - Temperature profiles of BIC components



4. Conclusion

This document presented the thermal analyses of the integrated assemblies composed of the electric motor and IIC power converter, and of the energy storage system and BIC converter. All the developed lumped parameter thermal models were implemented using the self-developed Python library *MuSA*, which exploits the network-like representation of the components to create an LPTN.

The first part of the document covered the development of three thermal networks modelling the electric motor integrated with the IIC, and a dedicated CFD model for the cooling jacket, which was primarily used to evaluate the convective HTC associated with the internal and external walls.

Hot-spot temperature results stemming from the three models were presented and compared. In all three cases, the highest temperature values associated with the windings, magnets, and power switches are well below their temperature limits, thus confirming the feasibility of the proposed integrated architecture from the thermal point of view. Given the close similarity between temperature results produced by the 3D single slot model and full 3D model, the former is deemed as the best compromise between modelling fidelity and computational and development.

Subsequently, the 3D single slot model was taken as a reference to perform a comprehensive sensitivity analysis, to evaluate possible improvements to the thermal performance of the assembly given by different choices of constitutive materials and by tighter manufacturing tolerances.

The second part of this document focused on integrating the energy storage system with the BIC by positioning them on two opposite sides of the cooling plate, which features two parallel serpentine channels, each containing 20 l/min of a 50:50 water-ethylene glycol mixture. The convective thermal resistance of the channel and the pressure gradient were evaluated by means of a periodic CFD simulation. An unsteady simulation using a WLTP drive cycle was performed to assess the maximum temperature of the various components. The maximum temperature reached by the modules is 35 °C while the maximum temperatures of the HVSC, LVSC and transformer are 25.67 °C, 29.38 °C and 105.05 °C respectively. The results confirm the effectiveness of the proposed cooling plate in managing the batteries and the BIC. However, possible improvements could be made to increase temperature uniformity at high C-rates.



5. References

5.1. SCAPE documents

- [1] D3.3 Configuration of the converter legs.

5.2. Citations

- [2] S. Busquets-Monge and L. Caballero. *IEEE Transactions on Industrial Electronics*, 66(1):25–36, 2019.
- [3] D. Staton, A. Boglietti, and A. Cavagnino. *IEEE Transactions on Energy Conversion*, 20(3):620–628, 2005.
- [4] I.S. Bjorklund and W.M. Kays. *Journal of Heat Transfer*, 81(3):175–183, 08 1959.
- [5] R. Wrobel, A. Griffo, and P.H. Mellor. 2012 XXth International Conference on Electrical Machines, pages 1424–1429, 2012.
- [6] M. Pastura, R. Notari, S. Nuzzo, D. Barater, and G. Franceschini. *IEEE Transactions on Transportation Electrification*, pages 1–1, 2023.
- [7] M. Pastura. PhD thesis– Alma Mater Studiorum– University of Bologna, 2023.
- [8] R. Rafiezadeh, S. Busquets-Monge, and S. Alepuz. 2023 *IEEE 32nd International Symposium on Industrial Electronics (ISIE)*, pages 1–8, 2023.
- [9] M. Pastura, R. Notari, S. Nuzzo, D. Barater, and G. Franceschini. 2022 *International Conference on Electrical Machines (ICEM)*, pages 1150–1155, 2022.
- [10] F. Menter. *AIAA Journal*, 32(8):1598–1605, 1994.
- [11] S. Patankar and D. Spalding. *Numerical prediction of flow, heat transfer, turbulence and combustion*, pages 54–73. Elsevier, 1983.
- [12] H. Weller, G. Tabor, H. Jasak, and C. Fureby. *Computers in Physics*, 12(6):620–631, 1998.
- [13] P.J. Roache. *Annual review of fluid Mechanics*, 29(1):123–160, 1997.
- [14] M. Seilmayer and V.K. K. *AIMS Electronics and Electrical Engineering*, 2(1):27, 2018.
- [15] S. Nategh, A. Krings, O. Wallmark, and M. Leksell. *IEEE Transactions on Industrial Electronics*, 61(11):5956–5965, 2014.
- [16] L. Marackova, V. Melcova, J. Samek, and O. Zmeskal. In *Chemistry and Life*, volume 955 of *Materials Science Forum*, pages 25–30. Trans Tech Publications Ltd, 6 2019.
- [17] S. Yamazaki, Y. Kurosaki, and T. Wakisaka. *Tetsu To Hagane–Journal Of The Iron And Steel Institute Of Japan*, 107(2):121–127, 2021.
- [18] R.W.A. LLC. <https://www.allianceorg.com/pdfs/PhysicalPropertiesofMagnets.pdf>, 2021.
- [19] Y. Kim, S. Mohan, J. B. Siegel, A. G. Stefanopoulou and Y. Ding. *IEEE Transactions on Control Systems Technology*, vol. 22, no. 6, pp. 2277–2286, Nov. 2014.
- [20] D. Bernardi, E. Pawlikowski and J. Newman. *ECS – The Electrochemical Society*, vol. 132, no. 1, pp. 5–12, Jan. 1985.
- [21] N. Zatta; B. De Cesaro; E. Dal Cin; G. Carraro; G. Cristofoli; A. Trovò; A. Lazzaretto and M. Guarnieri. *Batteries*, vol. 10, no. 7, 248, Jul. 2024





Funded by the European Union. Views and opinions expressed are however those of the author(s) only and do not necessarily reflect those of the European Union or CINEA. Neither the European Union nor the granting authority can be held responsible for them.



**Funded by
the European Union**